High Sensitivity and Rapid Response Optomechanical Uncooled Infrared Detector From Self-Assembled Super-Aligned Carbon Nanotubes Film

Peng Zhang, Huwang Hou, Zhendong Luo, Ye Feng, Hongmei Zhong, Hui Zhang, Ting Meng, and Yang Zhao

***Abstract*— The optomechanical uncooled infrared (IR) detector, characterized by a straightforward manufacturing process and sensitivity comparable to photonic detectors, employs bi-material microcantilevers as individual pixels. The detector's key performance parameters are thermomechanical sensitivity and time constant, which are directly proportional to the coefficient of thermal expansion (CTE) mismatch and thermal mass of the two materials. Carbon nanotubes (CNTs), which exhibit thermal contraction axially, have a CTE value of -11×10^{-6} K^{-1} around room temperature. When combined with metals, such as gold, which have a positive CTE, it is possible to create bi-material pixels with superior thermomechanical sensitivity. The low thermal mass nature of CNTs inherently endows the pixels with a rapid thermal response. To realize an optomechanical IR detector based on super-aligned CNTs, a microfabrication process was developed that incorporates a liquid-induced CNT self-assembled step. Theoretical analyses indicate that the thermomechanical sensitivity and response speed are doubled compared to traditional ceramic-metal based photomechanical uncooled IR detectors. The experimental results are in good agreement with the theoretical values, demonstrating a measured time constant and thermomechanical sensitivity of 62 ms and 0.466 μm/K, respectively. This design offers a viable path towards the development of high-performance uncooled IR detectors, facilitated by the integration of super-aligned CNTs. [2024-0011]**

***Index Terms*— Optomechanical uncooled infrared detector, bi-material cantilever, self-assembled super-aligned carbon nanotubes, thermomechanical sensitivity, response speed.**

Manuscript received 24 January 2024; revised 11 March 2024; accepted 29 March 2024. This work was supported in part by the National Natural Science Foundation of China under Grant 12172348 and Grant 12302251, in part by the National Key Research and Development Program of China under Grant 2022YFA1203604, and in part by the Research Projects of Department of Education of Guangdong Province under Grant 2022KQNCX227. Subject Editor C. Lee. *(Corresponding authors: Yang Zhao; Ting Meng.)*

Peng Zhang, Zhendong Luo, Hui Zhang, Ting Meng, and Yang Zhao are with the CAS Key Laboratory of Mechanical Behavior and Design of Materials, Department of Precision Machinery and Precision Instrumentation, University of Science and Technology of China, Hefei, Anhui 230027, China (e-mail: ustctm@ustc.edu.cn; yangz1@ustc.edu.cn).

Huwang Hou and Ye Feng are with the CAS Key Laboratory of Mechanical Behavior and Design of Materials, Department of Modern Mechanics, University of Science and Technology of China, Hefei 230022, China.

Hongmei Zhong is with the School of Mechanical and Electrical Engineering, Shenzhen Polytechnic University, Shenzhen, Guangdong 518055, China.

Color versions of one or more figures in this article are available at https://doi.org/10.1109/JMEMS.2024.3384497.

Digital Object Identifier 10.1109/JMEMS.2024.3384497

I. Introduction

INFRARED (IR) detection is a rapidly evolving field with applications in night vision, target tracking, non-contact thermometry, medical diagnosis, and space exploration [1]. Photonic IR detectors, which leverage the photoelectric effect, offer high sensitivity and rapid response, but their widespread use is limited due to the requirement for cryogenic cooling systems. To achieve room-temperature operation and cost-effectiveness, uncooled IR detectors, also known as thermal detectors, have been developed. These detectors convert absorbed IR radiation into a temperature rise, which is then converted into changes in physical parameters of thermal sensitive materials, such as resistance and capacitance, for signal readout. However, due to heat leakage through the readout integrated circuit (ROIC) [2], thermal detectors are significantly less sensitive than photonic detectors. To address this, new approaches using visible (VIS) detectors for IR detection have been explored [3], particularly optomechanical uncooled IR detectors based on bi-material microcantilevers [4], [5], [6].

The optomechanical mechanical uncooled IR detector, based on bi-material microcantilevers, represents a new generation of thermal detectors with sensitivity comparable to photonic detectors. Each pixel in these detectors typically consists of a bi-material microcantilever that undergoes bending motions upon absorbing IR radiation due to a mismatch in coefficient of thermal expansion (CTE) of the two materials, as shown in Fig. 1a. The bending motion allows the pixels to modulate the intensity of VIS light like micro mirrors, enabling the output of IR signals using VIS detectors instead of ROIC. The key functions of optomechanical mechanical uncooled IR detectors are thermomechanical sensitivity and time response, which are essential for signal-to-noise ratio and real-time detection. The selected materials for the bi-material microcantilever are crucial to meeting these requirements. Previous studies have mainly focused on ceramic-metal bi-material designs, but the thermomechanical sensitivity of these designs is limited by the inadequate CTE mismatch [7], [8], [9], [10], [11], [12]. A typical difference in thermal expansion coefficients of metal–ceramic bi-material is inherently limited to α<20 $\times$ 10^{-6} K^{-1} [13]. To overcome this limitation, new materials, such as polymer-metal bi-material design, have been explored [14], [15]. This new cantilever design

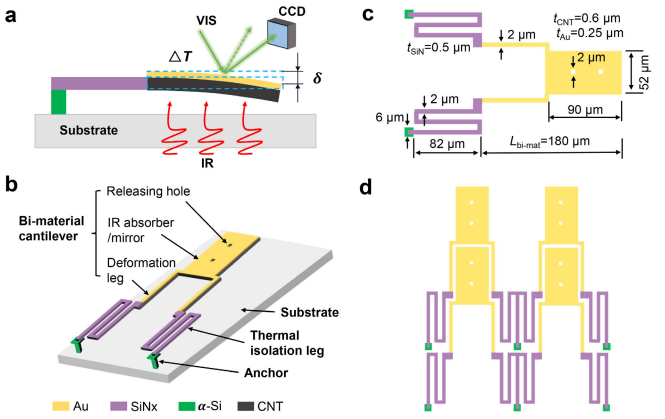

Fig. 1. **a**, The schematic diagram of the optomechanical uncooled infrared (IR) detector illustrates its working principle. Upon absorbing IR radiation, the bi-material cantilever's temperature rises. This temperature increase results in a bending motion due to the mismatch in thermal expansion coefficients of the two materials. This bending motion, in turn, functions like a micro-mirror, modulating the intensity of visible light. This allows for the detection of IR signals using visible light detectors. The proportionality between the intensity change in visible light and the amount of absorbed IR light enables accurate detection. **b**, Schematic diagram of the pixel structure. **c**, The geometric dimensions of the pixel. **d**, The double-stage nested layout of the pixels.

allows the achievement of nearly fourfold improvement in thermomechanical sensitivity compared to the ceramic-metal counterparts. However, due to the large thermal mass [16] and non-compatibility with traditional microfabrication technology [17] of the polymer, it has limitations in response speed and manufacturing process.

Carbon nanotubes (CNTs) possess exceptional thermal and mechanical properties that make them highly suitable for enhancing the performance of detectors. Specifically, CNTs exhibit a significantly negative CTE of approximately -11×10^{-6} K^{-1} along their axis at room temperature [13]. This unique property can be leveraged to increase the CTE mismatch, leading to improved thermal deformation sensitivity of the detector. Additionally, the extremely low thermal mass of carbon nanotubes contributes to enhancing the response speed of the detector. Moreover, a liquid-induced self-assembly process has been developed to produce a MEMS-compatible super-aligned CNT film with controlled orientation [18], enabling the effective utilization of their axial properties. Based on these considerations, the integration of CNTs into bi-material microcantilevers offers substantial benefits for optomechanical IR detectors. This paper aims to contribute to the understanding and optimization of CNT-based detectors for enhanced sensitivity and faster response, ultimately driving advancements in IR detection technology.

II. Working Principle

A. Materials and Structure

Fig. 1b illustrates the schematic design of a bi-material microcantilever pixel within an optomechanical uncooled infrared (IR) detector. Each pixel, anchored to a silicon substrate via two supports, comprises a bi-material cantilever and thermal isolation legs. The bi-material cantilever can be segmented into deformation legs and IR absorbers/mirrors, with release holes present on the IR absorbers/mirrors. The bi-material cantilever is constructed from stacked layers of gold on a closely packed, super-aligned CNT film. The CNT is MEMS-compatible and the detailed synthesis method for this CNT film is outlined in section III-A. IR radiation absorbed by the CNT layer at the bottom of IR absorber/mirror, after passing through the silicon substrate, is transformed into a temperature rise within the pixels. The top gold layer serves as a reflective mirror for visible light during optical readout. The back fold structure is utilized for thermal isolation legs, employing a layer of plasma-enhanced chemical vapor deposition (PECVD) low-stress silicon nitride with a low thermal conductivity, thereby minimizing heat dissipation from the pixel to the substrate. Additionally, low-pressure chemical vapor deposition (LPCVD) amorphous silicon, renowned for its pore-filling capabilities in the microfabrication process, is selected for the anchors.

TABLE I
Physical Properties of SiNx, Au and Super-Aligned CNT Film

	Density g/cm^3	Specific heat capacity J/(g·K)	Young's modulus Gpa	CTE ×10^{-6} K^{-1}	Thermal conductivity W/(m·K)
SiN_x	2.40	0.691	180	0.8	5.5
Au	19.30	0.129	73	14.2	296
CNT	0.46	0.730	150	-11	200

The physical parameters of silicon nitride and gold can be readily gleaned from previous studies focusing on optomechanical IR detectors utilizing ceramic-metal bi-material [12], [19]. The mass density of the CNT film is 0.46 g/cm^{-3} [18], the specific heat capacity is 730 J/(g· K) [20], and the CTE is approximately -11×10^{-6} K^{-1} along the axis at room temperature [13]. The thermal conductivity of CNT film is 200 W/(m·K) parallel to the alignment direction and 60 W/(m· K) perpendicular to the alignment direction [21]. In addition, the formation of the carbon nanotube (CNT) film is a complex process involving a vast array of interconnected CNTs, which are held together by the weak van der Waals force. This force is so weak that it allows for the occurrence of tube-to-tube slipping when the film is subjected to external force. Moreover, the thickness of the film is directly proportional to the number of CNTs present, thus a greater thickness enhances the probability of inter-tube slipping. Consequently, the Young's modulus of the CNT film is influenced by its thickness. Based on our previous research, the Young's modulus of the CNT film used in this study, after the application of a slipping suppression treatment, is approximately 150 Gpa [22]. Table I provides all these physical properties of SiNx, Au and super-aligned CNT film.

B. Heat Transfer Modeling

The pixel of the detector, as depicted in Fig. 1b, converts absorbed infrared radiation into thermal energy, causing a rise in itself temperature. The efficiency of this energy conversion

is determined by the absorptivity α of the absorber of the pixel, that is, the portion of absorbed radiation by the pixel. The energy conversion can be expressed by the following equation:

$$\alpha q = C_{\text{total}} \frac{\mathrm{d}\Delta T}{\mathrm{d}t} + G_{\text{total}} \Delta T \tag{1}$$

where q represents the net radiation power transferred to the pixel, which is given by the difference between the radiation power received from the object and the radiation power emitted by the pixel itself. C_{total} is the heat capacitance of the pixel, and G_{total} is the total thermal conductance. The temperature response of the pixel during the rise period:

$$\Delta T = \frac{q}{G_{\text{total}}} \left(1 - \exp\left(-\frac{t}{\tau}\right)\right) \tag{2}$$

with time constant

$$\tau = \frac{C_{total}}{G_{total}}. \tag{3}$$

The heat capacitance C_{total} is the summation of the thermal mass of all the structures in the pixel and calculated as

$$C_{\text{total}} = \sum\nolimits_i (\rho V c)_i \tag{4}$$

where ρ represents the material density, and c and V correspond to the specific heat and volume of the pixel, respectively. The index 'i' denotes each structure used in the pixel.

The G_{total} contains all heat exchange mechanisms of the detector, including the radiation G_{rad} between the pixel and environment, the thermal conduction through the thermal isolation legs G_{leg}, the thermal conduction by the air G_{air}, and the convection through the air gap between the pixel and substrate. Therefore, G_{total} can be expressed as follow:

$$G_{\text{total}} = G_{\text{leg}} + G_{\text{rad}} + G_{\text{air,cond}} + G_{\text{air,cov}} \tag{5}$$

The detector is engineered to absorb incident radiation energy. Kirchhoff's Law states that the amount of radiation absorbed by any object is equal to the amount of radiation emitted by that object. Consequently, the radiative interaction between the pixel and its surrounding environment is unavoidable. The radiation conductance serves as the ultimate lower limit for thermal conductance in the pixel and can be expressed as:

$$G_{\text{rad}} = 4\sigma A_{\text{pixel}} \varepsilon T^3 \tag{6}$$

where A_{pixel} is the total area of pixel surface, σ the Stefan-Boltzman constant, and ε ($\varepsilon = \alpha$) is the emissivity (absorptivity) of the cantilever materials.

The thermal conductance of the thermal isolation legs is a function of the leg geometry and the thermal conductivity of the leg materials:

$$G_{\text{leg}} = \frac{W_{\text{leg}} t_{\text{leg}} k_{\text{leg}}}{L_{\text{leg}}} \tag{7}$$

in which, W_{leg} is the width of the leg cross-section, t_{leg} the height (thickness) of the leg cross-section, L_{leg} the total length of the leg, and k_{leg} is the thermal conductivity of the leg material.

The air thermal conduction is expressed as

$$G_{\text{air,cond}} = \frac{k_{\text{air}} A_{\text{pixel}}}{d_{\text{gap}}} \tag{8}$$

where k_{air} is the thermal conductivity of air, with a value of 0.026 W/(m· K) at atmospheric pressure. The d_{gap} represents the gap distance between the pixel and substrate. Under the atmospheric pressure, the thermal conductance of the air gap is 3∼4 orders of magnitude higher than that of radiation. Therefore, the uncooled IR detectors must operate in a vacuum environment to suppress the dissipation of heat signals by air. Furthermore, due to the vacuum working environment, both air convection and air heat conduction can be neglected. Hence, the total thermal conductance G_{total} can be simplified from equation (5) as:

$$G_{\text{total}} = G_{\text{leg}} + G_{\text{rad}}. \tag{9}$$

As indicated in the above, the G_{total} has a strong effect on the performance of the detector. To achieve a substantial temperature rise, it is crucial to minimize the total heat conductance G_{total}. However, the time constant τ is reversely proportional to the total thermal conductance G_{total}. Consequently, there exists a trade-off between the response speed and the sensitivity of the detector.

C. Temperature-Dependent Deformation

For the proper operation of the detector, the transduction of temperature rise into thermally induced deflection is crucial. The thermomechanical sensitivity S is defined below:

$$S = \frac{\delta}{\Delta T} = 3(\alpha_1 - \alpha_2) \left(\frac{n+1}{K}\right) \left(\frac{L_{\text{bi-mat}}^2}{t_2}\right) \tag{10}$$

$$K = 4 + 6n + 4n^2 + \phi n^3 + \frac{1}{\phi n} \tag{11}$$

$$n = \frac{t_1}{t_2}, \quad \phi = \frac{E_1}{E_2} \tag{12}$$

in which δ is the temperature-induced deflection at the free-end of bi-material cantilever, E the Young's modulus, and α is the CTE of the cantilever materials. The t represents the thickness of each layer, and $L_{\text{bi-mat}}$ is the length of the bi-material cantilever. The key point can be highlighted again from (10), the CTE mismatch of the two selecting materials must be large. In addition, for given materials and $L_{\text{bi-mat}}$, the thermomechanical sensitivity S is directly proportional to the function $f(n)$ of thickness ratio n, which can be denoted by:

$$f(n) = \frac{n+1}{K} = \frac{n+1}{4 + 6n + 4n^2 + \phi n^3 + \frac{1}{\phi n}} \tag{13}$$

Thus, the optimization of n maximizes $f(n)$, which is dependent on $E_{\text{Au}}/E_{\text{CNT}}$ and theoretically predicted to be $n = 0.4$.

D. Geometry and Layout

Based on the above design analysis, Fig. 1c reveals the geometric dimensions of pixels, with detailed parameters are listed in Table II. Additionally, Fig. 1d illustrates a schematic

TABLE II
GEOMETRIC PARAMETERS OF THE PIXEL STRUCTURE

Bi-material type	Pixel size [μm]	L_{leg} [μm]	W_{leg} [μm]	t_{leg} [μm]	L_{bi-mat} [μm]	t_{Au} [μm]	t_{CNT} [μm]	t_{SiN} [μm]
CNT-Au	100	240// 240	2	0.5	180	0.25	0.6	/
SiNx-Au	100	240// 240	2	0.5	180	0.25	/	0.6

'//' indicates a parallel thermal resistance relationship of thermal isolation legs.

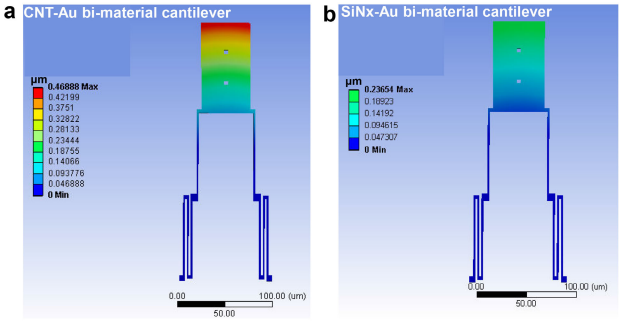

Fig. 2. **a**, Thermomechanical deformation simulation of CNT-Au bi-material cantilever. **b**, Thermomechanical deformation simulation of SiNx-Au bi-material cantilever.

TABLE III
PERFORMANCE PARAMETERS OF THE PIXEL STRUCTURE

Bi-material type	G_{total} [W/K] x 10^{-8}	C_{total} [J/K] x 10^{-9}	τ [ms]	S [μm/K]
CNT-Au	8.69	5.24	60	0.469
SiNx -Au	8.69	9.54	110	0.24

diagram of the pixel layout, employing a double-stage nested design to enhance space utilization. To highlight the benefits of utilizing super-aligned CNT in optomechanical infrared detectors, theoretical calculations were conducted on the performance parameters of two types of pixels with identical dimensions but differing materials. The A-type pixel featured a bi-material cantilever with CNT-Au, while the B-type pixel utilized the conventional SiNx-Au bi-material cantilever structure. The thermal isolation legs of both A-type and B-type pixels shared the same structure, geometric dimensions, and material. The thermal conductance and thermal capacitance were calculated based on the pixel's geometric dimensions and material physical parameters, with the time constant subsequently derived from these. A steady-state simulation using ANSYS yielded the thermomechanical sensitivity of the pixel. As depicted in Fig. 2, applying a temperature load of 1°C difference from the environment on the pixel cantilever results in deformation, representing the thermomechanical sensitivity. Table III lists the thermal conductance, thermal capacitance and performance parameters of A-type and B-type pixels under this design. It is evident that the thermomechanical sensitivity of the A-type pixel (CNT-Au bi-material cantilever) is approximately 1 times higher than that of the B-type pixel (SiNx-Au bi-material cantilever), and the response time has been reduced by half.

TABLE IV
PERFORMANCE PARAMETERS FOR SEVERAL BI-MATERIAL CANTILEVER WORKS

References	Pixel size[μm]	Bi-material type	τ [ms]	S [μm/K]	FOM [m•K•s]
[14]	200	polymer-Au	86	0.3	0.11
[12]	100	SiNx - Au	80	0.11	0.073
This work	100	CNT-Au	60	0.469	0.013

Furthermore, in the paper that first introduced the optomechanical uncooled IR detector globally, the thermomechanical sensitivity of the detector with a 100 μm pixel size was 0.11 μm/K [12]. In comparison, the thermomechanical sensitivity of a super-aligned CNT based detector with the same pixel size is nearly 3 times higher. Considering the correlation between pixel size and thermomechanical sensitivity, the larger the pixel size, the greater the thermomechanical sensitivity. The thermomechanical sensitivity of the bi-material cantilever detector based on polymers with a 200 μm pixel size is 0.3 μm/K [14]. This is lower than the thermomechanical sensitivity of the detector with a 100 μm pixel size here. It is crucial to highlight that in these studies, the variations in performance parameters exhibited by the detectors are partially attributable to distinct pixel structure designs. To facilitate direct comparison of the thermomechanical sensitivity and time constant of detectors with varying materials, structures, and pixel sizes, we can normalize the pixel sizes and propose a Figure of Merit (FOM). The FOM is given by

$$\text{FOM} = \frac{\tau}{S/p^2} \tag{14}$$

where the p is the pixel size and FOM has units of (m· K· s). A small FOM is better than a large FOM. Table IV presents a comparative analysis of performance parameters for several bi-material cantilever works.

III. EXPERIMENTAL RESULTS

A. Synthesis of Super-Aligned Carbon Nanotubes Film

Currently, the synthesis of vertically aligned carbon nanotube (VACNT) forests through water-assisted chemical vapor deposition (CVD) has reached a high level of maturity [23]. Building upon this, the self-assembled super-aligned CNT film has been successfully prepared [18], [24]. Fig. 3a illustrates the steps of the self-assembly scheme. First, a strip catalyst array on a substrate was patterned using conventional UV lithography and etching. The catalyst consists of 2 nm thermal evaporation Fe with a 10 nm atomic layer deposition (ALD) Al_2O_3 buffer layer underneath. Subsequently, the VACNT sheets, as depicted by double-headed arrows indicating alignment direction in Fig. 3b, are synthesized via the water-assisted CVD from the patterned strip catalyst. The VACNT is a very sparse material, with nanotubes occupying only 1% of the total volume. This is evident in Fig. 3c, which offers an enlarged SEM image of the sidewall of the VACNT sheets shown in Fig. 3b, highlighting the sparsity of VACNTs.

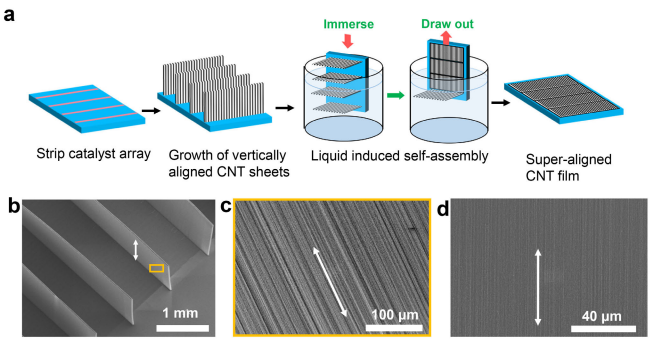

Fig. 3. **a**, A vertically aligned CNT (VACNT) sheets array were synthesized from strip catalysts and folded into a closely packed, horizontally aligned CNT film through a liquid induced self-assembly process. **b**, SEM image of the vertically aligned CNT sheets array. Double-headed arrow indicates CNT alignment direction. **c**, Enlarged SEM image of the sidewall of the VACNT sheets, showing the sparse of VACNTs. **d**, SEM image of horizontally aligned CNT film, showing the closely packed characteristics.

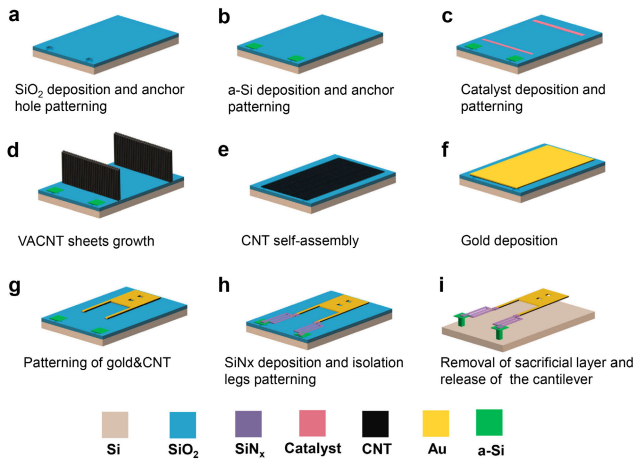

Fig. 4. Microfabrication process of optomechanical uncooled IR detector from self-assembled super-aligned CNT.

Following this, the VACNT sheets were immersed in an isopropyl alcohol (IPA) solution and then carefully draw out, enabling the folding of the vertically aligned CNT sheets into horizontally aligned CNT. This folding process was achieved through the surface tension at the gas-liquid interface, inducing a buckling instability in the VACNT sheets. Finally, the liquid was evaporated by allowing the substrate to dry under ambient conditions. During this drying process, the liquid capillary force and van der Waals force effectively assembled the sparse CNTs into a closely packed, highly aligned CNT film (Fig. 3d) where photoresists could be uniformly coated on because of the flatness of the film surface [25]. The volume density of the CNT film is about 50%. The thickness of the CNT film is proportional to the width of the strip catalyst. Furthermore, the cohesion between individual CNTs and the adhesion between the CNT film and the substrate are sufficient to withstand lithographic processes including heat treatment and immersion into liquids. Thus, a MEMS-compatible CNT film was successfully prepared.

B. Microfabrication and Characterization

The optomechanical uncooled IR detector is constructed with a 10 × 10 pixel array, tiled in a pattern with a 100 μm × 100 μm pitch. A microfabrication process has been developed and a brief explanation is shown in Fig. 4. This process consists of five masking steps and started with a double side polished silicon wafer with thickness of 500 μm. Firstly, a 2.5 μm silicon dioxide layer was deposited on the wafer surface as the sacrificial layer using PECVD, and the anchor holes array in the sacrificial layer were patterned. Secondly, a LPCVD amorphous silicon film with a thickness of 1 μm was deposited onto the wafer, and the anchors patterning was followed. Then the formation of a super-aligned CNT film was achieved through the processes described in section III-A, including catalyst deposition and patterning, VACNT sheets growth, and liquid-induced CNT self-assembly. The width of the strip catalyst is 30 μm and the thickness of the CNT film is 600 nm. Following this, a gold film 250 nm thick was deposited by sputtering onto the super-aligned CNT film, forming a CNT-Au bi-material film. To promote adhesion between the gold and CNT film, a 50-nm-thick Cr film was deposited on the CNT film prior to Au sputtering. Given the identical planar geometric dimensions of Au and CNT structures, a common photoresist pattern was utilized as a mask to sequentially etch both the Au film and CNT film by ICP. This process defined the bi-material cantilevers. Specifically, Cl_2 was employed as the etching gas for the Au film, while O_2 was utilized for the CNT film. Two release holes were evenly opened in the absorber/mirror of the bi-material cantilever to facilitate removal of the sacrificial layer under the structure in the subsequent release step. Afterwards, a low-stress silicon nitride of 500 nm thickness was deposited by PECVD and patterned into the back fold thermal isolation legs. The two ends of the thermal isolation legs served to cover portions of the bi-material cantilever and the anchor, respectively, thereby facilitating a connection between the separate anchor and the bi-material cantilever. Finally, the underlying sacrificial layer was removed by wet etching in a 49% HF solution for 2.5 minutes, thereby releasing the cantilevers. Following a series of ethanol rinsed with increasing concentration from 50% to 100%, the sample was then dried in a critical point dryer to prevent the cantilevers from sticking to the substrate under capillary action. In addition, our previous investigations of the mechanical properties and thermal response of the CNT based microcantilevers indicate that the sliding between the tubes due to weak van der Waals interaction limits the thermo-mechanical sensitivity of the bi-material microcantilevers [22]. Therefore, following the critical point drying process, an inter-tube deposition of 10 nm Al_2O_3 thin film by ALD was used to reinforce the binding between the tubes. At this point, the optomechanical mechanical uncooled IR detector from self-assembled super-aligned CNT film was successfully prepared.

Fig. 5a and Fig. 5b illustrate the top-view and side-view SEM images of the microcantilever array in the detector. Fig. 5b reveals a degree of non-uniformity and bending in the bi-material cantilevers, which deviate from the silicon substrate. This bending was attributed to residual stress in the thin films, which included the intrinsic stress gradient across the CNT and Au films, as well as the thermal stress between these two films due to mismatch in thermal expansion. Based on our experimental tests, we have observed that replacing

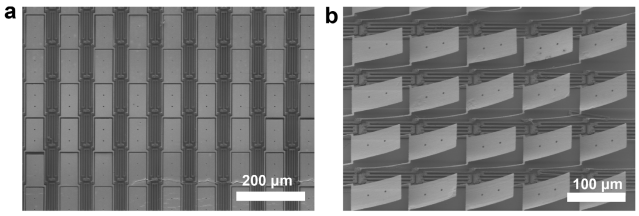

Fig. 5. **a**, Top view SEM image of microcantilever array. **b**, Side-view SEM image of microcantilever array.

sputtering with thermal evaporation for gold deposition can reduce the degree of bending.

C. Measurement of Time Constant

Fig. 6a illustrates the schematic design of an optical readout system, employing knife-edge filtering, for the measurement of the time constant of optomechanical IR detectors. The detector chip is packed in a custom-built vacuum chamber, maintained at a pressure of 0.1 Pa, to eliminate the impact of air heat transfer. The temperature of the detector chip is stabilized by four uniformly distributed thermoelectric coolers (TEC) inside the chamber. On either side of the vacuum chamber, there are installed IR and visible light windows. The IR radiation, modulated by a chopper, is collected by an IR lens and incident onto the detector chip inside the chamber. Simultaneously, a 532nm laser, serving as readout light, is obliquely directed onto the IR detector from the opposite side of the chamber, after passing through a beam expander. The reflected diffracting rays, synthesizing the spectra of the gold mirrors of the detector pixel array, are analyzed by a conventional charge-coupled device (CCD). When the incident IR radiation is absorbed by the pixels, the temperature of the detector chip rises, leading to a small deflection of the cantilevers, and consequently, a shift in the reflected readout light. This results in a variation in the amount of readout light passing through the knife-edge, subsequently affecting the intensity of readout light received by the CCD. Consequently, the IR signal is converted into a visible signal, and the readout is based on the gray value of the CCD. Fig. 6b shows the real optical readout system.

From (2), it can be inferred that, for a square-wave pulse of radiation modulated by the chopper, the change in detector temperature T exhibits an exponential rise and decay with a time constant τ. Thus, the gray value of CCD also exhibits an exponential rise and decay during pulsed heating and subsequent cooling process. Fig. 6c illustrates the variation in CCD gray values in response to the modulated IR signal. The fit curves of the signal rise and decay, modeled by exponential functions, yielded a time constant of 62 ms, which closely aligns with the theoretical value of 60 ms. Additionally, due to partial damage to the chopper blades used in the experiment, the structural symmetry of the chopper was disrupted, resulting in different time periods for the rise and decay stages of the gray value.

It is worth noting that the mentioned result was observed under the condition where the incident IR was in the long wavelength infrared (LWIR) band range of 8-14 μm. From (1), the spectral dependence of the responsivity of uncooled

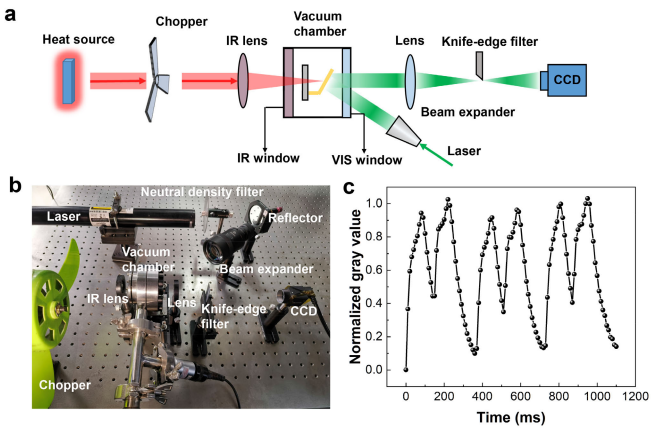

Fig. 6. **a**, Schematic diagram of an optical readout system based on knife edge filtering for testing the time constant of optomechanical IR detectors. The detector chip is packed in a vacuum chamber to eliminate the effect of air heat transfer. The IR radiation, modulated by a chopper to form square-wave pulse, is collected by an IR lens and incident onto the detector chip. Visible light (readout light) that comes from the laser is reflected by the pixels of the detector and then collected by a lens. It then passes through a knife-edge filter and analyzed by a conventional CCD. **b**, The real optical readout system. **c**, The variation of CCD gray values with the modulated IR signal. For a square-wave pulse IR radiation, the gray values of CCD show exponential increase and decrease, from which the time constant can be inferred.

infrared detectors is determined by the spectral distribution of the absorptivity $\alpha(\lambda)$. Considering the high absorptivity of CNT across a broad spectrum ranging from near infrared (NIR) to LWIR [26], and even into the terahertz band [27], theoretically, this detector can operate over a broad spectrum. Here, the experiment spectrum was selected by the IR lens and IR windows. Given that the response time and thermomechanical sensitivity of the detector are governed by the pixel structure, these intrinsic parameters remain unaltered when operating in other spectrums. Nevertheless, considering the variability in the absorptivity of CNT across different spectra, there are discrepancies in the conversion efficiency of the net radiated power of the detector, resulting in variations in temperature rise.

D. Measurement of Thermomechanical Sensitivity

The thermomechanical sensitivity of an optomechanical IR detector is assessed using the system depicted in Fig. 7a. The detector is heated by a TEC under the control of a TEC controller. The temperature at the sample surface is monitored using a thermocouple, and the thermocouple signal is read by the TEC controller to achieve closed-loop temperature control of the sample. The deformation profiles of the pixels at varying temperatures are recorded using a white-light interferometer, which is capable of measuring the 3D morphology of nanoscale structures.

One of the profile images of IR detector pixels, obtained from the above system, is displayed in the inset of Fig. 7a. These images allow for the extraction of the vertical deflection δ of the bi-material cantilever at a position y along its length L. Fig. 7b presents the deflection data for one of the bi-material cantilevers, ranging from 25 °C to 31 °C with an interval of 2 °C. The dots represent measured data, while the lines are quadratic polynomial fits. The zoom-in inset in Fig. 7b provides the profiles of the bi-material cantilever ends

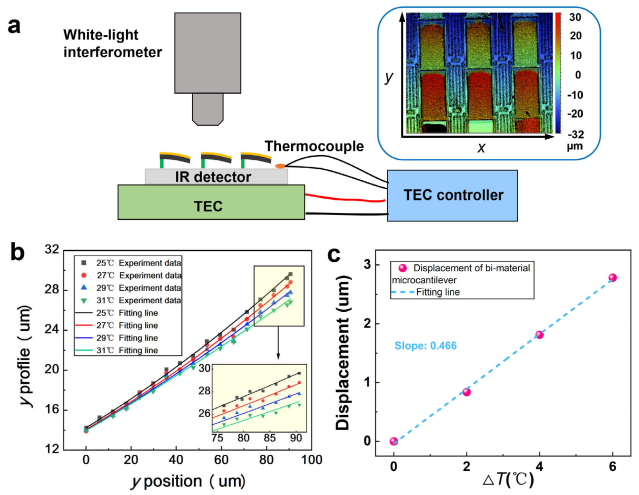

Fig. 7. **a**, Schematic diagram of the experimental set-up for thermomechanical sensitivity measurement. The detector is heated by a TEC under the control of a TEC controller. The deformation profiles of the pixels of detector at different temperature are recorded by a white-light interferometer. Inset: the profile image of IR detector pixels **b**, The deformation profiles of the bi-material cantilever at a position y along its length L. Inset: enlarged profiles of the bi-material cantilever ends. **c**, The deflection values at the bi-material cantilever ends as a function of temperature.

at each temperature. According to (10), the thermomechanical sensitivity of the IR detector is represented by the slope, which is determined through linear fitting of the deflection values δ at the bi-material cantilever ends for each temperature, as shown in Fig. 7c. The fitting result reveals a thermomechanical sensitivity of 0.466 μm/K, which also closely aligns with the simulation value of 0.469 μm/K.

IV. Conclusion

Overall, we have demonstrated the design, fabrication and performance of an optomechanical uncooled IR detector based on self-assembled super-aligned CNT film. The theoretical and experimental evidence suggests that CNT-based detectors outperform traditional ceramic-metal detectors in terms of thermomechanical sensitivity and response speed. It is worth mentioning that when designing uncooled IR detectors, it is essential to strike a balance between the two key parameters. These two parameters are often challenging to improve simultaneously. In the study presented here, we have successfully mitigated this design trade-off to a certain extent at the material level. Therefore, the successful integration of self-assembled super-aligned CNTs into bi-material microcantilevers opens up new possibilities for achieving high-performance uncooled IR detectors.

Future research efforts may focus on further improving the fabrication process to achieve small pixel size, large arrays, and better uniformity of microcantilevers. The pixel size here is 100 μm, primarily restricted by the processing accuracy of the contact ultraviolet (UV) lithography machine utilized in the experiment. By employing a deep ultraviolet (DUV) stepper projection aligner, it becomes feasible to further diminish the pixel size within the diffraction limit of the infrared spectrum. For LWIR, the minimum attainable pixel size approximates 8 μm. Nevertheless, similar to other uncooled IR detectors, this advancement presents the challenge of diminishing sensitivity associated with reducing pixel size. Consequently, achieving smaller pixel sizes requires not only the use of more accurate processing apparatus but also calls for innovative pixel structure designs. Such designs could include multi-layer configurations that segregate thermal isolation and thermal deformation from the optical fill factor (the ratio of the absorber area to the entire pixel area) for improved sensitivity. Additionally, the integration of micro-lens arrays presents a viable approach to enhance the optical fill factor.

Acknowledgment

This work was partially carried out at the USTC Center for Micro and Nanoscale Research and Fabrication, and the Experimental Center of Engineering and Material Sciences, USTC.

References

[1] Q. Shen et al., "Bioinspired infrared sensing materials and systems," *Adv. Mater.*, vol. 30, no. 28, Jul. 2018, Art. no. 1707632.
[2] J. Zhao, "High sensitivity photomechanical MW-LWIR imaging using an uncooled MEMS microcantilever array and optical readout," *Proc. SPIE*, vol. 5783, pp. 506–513, May 2005.
[3] W. Chen et al., "Continuous-wave frequency upconversion with a molecular optomechanical nanocavity," *Science*, vol. 374, no. 6572, pp. 1264–1267, Dec. 2021.
[4] H. Zhu et al., "A terahertz optomechanical detector based on metasurface and bi-material micro-cantilevers," *Micromachines*, vol. 13, no. 5, p. 805, May 2022, doi: 10.3390/mi13050805.
[5] Z. Luo, H. Hou, Y. Zhang, W. Li, P. Zhang, and Y. Zhao, "Optimal design of optomechanical uncooled infrared focal plane array with integrated metalens," *Phys. Scripta*, vol. 99, no. 1, Jan. 2024, Art. no. 015510.
[6] H. Hou, Y. Zhang, Z. Luo, P. Zhang, and Y. Zhao, "Design and fabrication of monolithically integrated metalens for higher effective fill factor in long-wave infrared detectors," *Opt. Lasers Eng.*, vol. 150, Mar. 2022, Art. no. 106849.
[7] Y. Zhao, J. Choi, R. Horowitz, A. Majumdar, J. E. Kitching, and P. R. Norton, "Characterization and performance of optomechanical uncooled infrared imaging system," *Proc. SPIE*, vol. 4820, pp. 164–174, Jan. 2003.
[8] W. Ma, R. Zhao, S. Wang, X. Yu, Y. Feng, and Y. Zhao, "Bimaterial cantilever focal plane array for uncooled infrared imaging using sandwich-framed structure," *J. Microelectromech. Syst.*, vol. 25, no. 2, pp. 413–420, Apr. 2016.
[9] Y. Wen et al., "Photomechanical meta-molecule array for real-time terahertz imaging," *Microsyst. Nanoeng.*, vol. 3, no. 1, pp. 1–7, Dec. 2017.
[10] D. Grbovic, N. V. Lavrik, S. Rajic, and P. G. Datskos, "Arrays of SiO_2 substrate-free micromechanical uncooled infrared and terahertz detectors," *J. Appl. Phys.*, vol. 104, no. 5, Sep. 2008, Art. no. 054508.
[11] F. Dong et al., "An uncooled optically readable infrared imaging detector," *Sens. Actuators A, Phys.*, vol. 133, no. 1, pp. 236–242, Jan. 2007.
[12] Y. Zhao et al., "Optomechanical uncooled infrared imaging system: Design, microfabrication, and performance," *J. Microelectromech. Syst.*, vol. 11, no. 2, pp. 136–146, Apr. 2002.
[13] Y.-K. Kwon, S. Berber, and D. Tománek, "Thermal contraction of carbon fullerenes and nanotubes," *Phys. Rev. Lett.*, vol. 92, no. 1, Jan. 2004, Art. no. 015901.
[14] Y. Shang, X. Ye, M. Wang, P. Song, and J. Feng, "Design, fabrication, and characterization of a polymer-based MEMS uncooled infrared focal plane array," *J. Microelectromech. Syst.*, vol. 24, no. 4, pp. 1132–1141, Aug. 2015.
[15] Y. Shang, X. Ye, L. Cao, P. Song, and J. Feng, "Coaxial dual-wavelength interferometric method for a thermal infrared focal-plane-array with integrated gratings," *Sci. Rep.*, vol. 6, no. 1, pp. 1–10, May 2016.
[16] J. Yao, Y. Yao, and T. Liu, "'Fire-beetles' inspired all-solid infrared sensor with bolometric and photomechanic dual sensing modes," *Mater. Design*, vol. 230, Jun. 2023, Art. no. 111968.
[17] A. Rogalski, *Infrared and Terahertz Detectors*, 3rd ed. Boca Raton, FL, USA: CRC Press, 2019, pp. 207–213.
[18] Y. Hayamizu et al., "Integrated three-dimensional microelectromechanical devices from processable carbon nanotube wafers," *Nature Nanotechnol.*, vol. 3, no. 5, pp. 289–294, May 2008.

[19] X. Yu et al., "Design and fabrication of a high sensitivity focal plane array for uncooled IR imaging," *J. Micromech. Microeng.*, vol. 18, no. 5, May 2008, Art. no. 057001.
[20] H. Zhan, Y. W. Chen, Q. Q. Shi, Y. Zhang, R. W. Mo, and J. N. Wang, "Highly aligned and densified carbon nanotube films with superior thermal conductivity and mechanical strength," *Carbon*, vol. 186, pp. 205–214, Jan. 2022.
[21] B. Chen et al., "Highly polarization-sensitive far infrared detector based on an optical antenna integrated aligned carbon nanotube film," *Nanoscale*, vol. 12, no. 22, pp. 11808–11817, 2020.
[22] P. Zhang et al., "Highly aligned carbon nanotube-based bi-material microactuators with reduced intertube slipping," *ChemNanoMat*, vol. 6, no. 3, pp. 404–411, Mar. 2020.
[23] A. Cao, P. L. Dickrell, W. G. Sawyer, M. N. Ghasemi-Nejhad, and P. M. Ajayan, "Super-compressible foamlike carbon nanotube films," *Science*, vol. 310, no. 5752, pp. 1307–1310, Nov. 2005.
[24] H. Zhang, Y. Wang, P. Zhang, H. Hou, and Y. Zhao, "Investigation and optimization of polarization properties of self-assembled carbon nanotube films," *Nanotechnology*, vol. 33, no. 19, May 2022, Art. no. 195702.
[25] T. Yamada et al., "Hierarchical three-dimensional layer-by-layer assembly of carbon nanotube wafers for integrated nanoelectronic devices," *Nano Lett.*, vol. 12, no. 9, pp. 4540–4545, Sep. 2012.
[26] Y. Jin et al., "Broadband omnidirectional perfect absorber based on carbon nanotube films," *Carbon*, vol. 161, pp. 510–516, May 2020.
[27] L. Ren et al., "Collective antenna effects in the terahertz and infrared response of highly aligned carbon nanotube arrays," *Phys. Rev. B, Condens. Matter*, vol. 87, no. 16, Apr. 2013, Art. no. 161401.

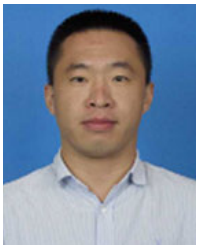

Peng Zhang received the B.S. degree in mechanical engineering from China University of Mining and Technology, China, in 2016, and the Ph.D. degree in instrument science and technology from the University of Science and Technology of China, China, in 2021. He is currently a Post-Doctoral Researcher with the Department of Precision Machinery and Instrumentation, University of Science and Technology of China. His research interests include the design and fabrication of MEMS and optical detection techniques.

Huwang Hou received the B.S. and Ph.D. degrees in mechanical engineering from the University of Science and Technology of China, China, in 2018 and 2023, respectively. His research interests include the design and fabrication of MEMS and metalens technology.

Zhendong Luo received the B.S. degree in engineering (measurement and control technology and instruments) from the University of Science and Technology of China (USTC), Hefei, China, in 2021. He is currently pursuing the joint Ph.D. degree in instrument technology engineering and electrical engineering with the University of Science and Technology of China and the City University of Hong Kong. His research interests include infrared detection and metalens technology.

Ye Feng received the bachelor's degree in medicine from Anhui University of Chinese Medicine in 2017, the master's degree in medicine from Guangzhou University of Chinese Medicine in 2020, and the Ph.D. degree in pharmacology of traditional Chinese medicine from Anhui University of Chinese Medicine in 2023. She is currently a Post-Doctoral Researcher with the School of Engineering Sciences, University of Science and Technology of China. Her research interests include the traditional mechanism of traditional Chinese medicine and organ-on-a-chip.

Hongmei Zhong received the Ph.D. degree in mechanical engineering from the City University of Hong Kong in 2021. She is currently a Lecturer with Shenzhen Polytechnic University, China. Her research interests include radiative cooling and thermal management.

Hui Zhang received the B.S. degree from Dalian Maritime University, China, in 2018, and the Ph.D. degree in instrument science and technology from the University of Science and Technology of China, China, in 2023. His research interests include polarization optics and carbon nanotube technology.

Ting Meng received the B.S. degree from Shandong University, China, in 2017, and the Ph.D. degree from the University of Science and Technology of China, China, in 2022. Since 2022, she has been a Post-Doctoral Researcher with the Department of Precision Machinery and Instrumentation, University of Science and Technology of China. Her current research interests include micro- and nano-scale heat transfer.

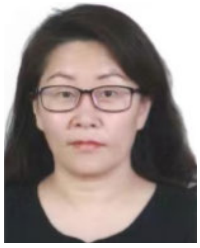

Yang Zhao received the B.S. and M.S. degrees in mechanical engineering from the University of Science and Technology of China, China, in 1994 and 1997, respectively, and the Ph.D. degree in mechanical engineering from the University of California at Berkeley in 2002. She is currently a Professor with the Department of Precision Machinery and Instrumentation, University of Science and Technology of China. Her current research interests include micro/nano-scale heat transfer, design and fabrication of MEMS, metalens technology, and nanomaterials.